Autonomous stabilization with programmable stabilized state

Ziqian Li[†,1,2,3] Tanay Roy[†,*,1,2] Yao Lu,[1,2,*] Eliot Kapit,[4] and David I. Schuster[1,2,5,3]

[1]*James Franck Institute, University of Chicago, Chicago, Illinois 60637, USA*
[2]*Department of Physics, University of Chicago, Chicago, Illinois 60637, USA*
[3]*Department of Applied Physics, Stanford University, Stanford, California 94305, USA*[†]
[4]*Department of Physics, Colorado School of Mines, Golden, CO 80401*
[5]*Pritzker School of Molecular Engineering, University of Chicago, Chicago, Illinois 60637, USA*
(Dated: December 19, 2023)

Reservoir engineering is a powerful technique to autonomously stabilize a quantum state. Traditional schemes involving multi-body states typically function for discrete entangled states. In this work, we enhance the stabilization capability to a continuous manifold of states with programmable stabilized state selection using multiple continuous tuning parameters. We experimentally achieve 84.6% and 82.5% stabilization fidelity for the odd and even-parity Bell states as two special points in the manifold. We also perform fast dissipative switching between these opposite parity states within 1.8 μs and 0.9 μs by sequentially applying different stabilization drives. Our result is a precursor for new reservoir engineering-based error correction schemes.

I. INTRODUCTION

Entanglement is one major resource any quantum protocol utilizes to achieve quantum advantage [1, 2]. Generally, the entanglement is created by unitary operations, where dissipation is considered detrimental and should be maximally avoided. Inspired by laser cooling, an alternative approach is to use tailored dissipation for stabilizing entanglement. By coupling the qubit system to some cold reservoirs, one can engineer the Hamiltonian such that the population will flow directionally to the stabilized point in the Hilbert space, and extra entropy is autonomously dumped into the cold reservoir during the process. This provides an extra route to state preparation. In a multiqubit-reservoir coupled system, dissipation engineering can enhance the capabilities of quantum simulation, as predicting the final state of a driven dissipative quantum system is more complex than its unitary counterpart [3] when all local qubit and reservoir interactions are simultaneously turned on. Dissipation stabilization also inspires autonomous quantum error correction codes (AQEC) [4–9] that achieve hardware efficiency in the experiment.

Stabilization has been theoretically proposed and experimentally realized in different platforms, such as superconducting qubits [10–17] and trapped ions [18, 19], focusing on stabilizing a single special state per device, such as even or odd parity Bell states. Unlike universal quantum state preparation through unitary gate decomposition, dissipative stabilization requires individual Hamiltonian engineering for each stabilized state through different drive combinations or hardware. This makes the tunable dissipative stabilization a challenging task.

A generalized scheme that allows one to programmatically choose stabilized states from a large class of states per device will expand the toolbox for state preparation. For instance, the ability to choose an arbitrary stabilized state can be used for the implementation of density matrix exponentiation [20, 21] by enabling an efficient reset of the input density matrix.

In this work, we realize an autonomous stabilization protocol with superconducting circuits that allows selection from a broad class of states, including the maximally entangled states. We use microwave-only drives with tunable parameters such as drive detunings and strengths that allow fast programmable switching between Bell states of different parities. The system is based on a two-transmon inductive coupler design [8, 17, 22, 23] that allows fast parametric interactions between qubits without significantly compromising their coherence. The readout resonators are also used as cold reservoirs, eliminating the requirement for extra components. We perform stabilization spectroscopy and demonstrate a fidelity over 78% for all stabilized states. For odd and even parity Bell pairs, we measured 84.6% and 82.5% stabilization fidelity and a stabilization time of 1.8 μs and 0.9 μs respectively. The structure of the paper is as follows. First, we explain the Hamiltonian construction of the stabilization protocol. Then we discuss the experimental measurement of individual stabilized state and demonstrate a dissipative switch of Bell state parity.

II. STABILIZATION THEORY

We consider a system of two coupled qubit-resonator pairs $\{Q_1, Q_2\}$ and $\{R_1, R_2\}$. The lossy resonators serve as both cold baths and dispersive readouts for the qubits. We label the ground and the first excited states of the qubits $Q_{1/2}$ as $|g\rangle$ and $|e\rangle$, and of the resonators $R_{1/2}$ as $|0\rangle$ and $|1\rangle$, with the full system state being represented as $|Q_1 Q_2 R_1 R_2\rangle$. The system Hamiltonian $H_{\text{sys}} = H_{QQ} + H_{QR1} + H_{QR2}$ includes the dominant
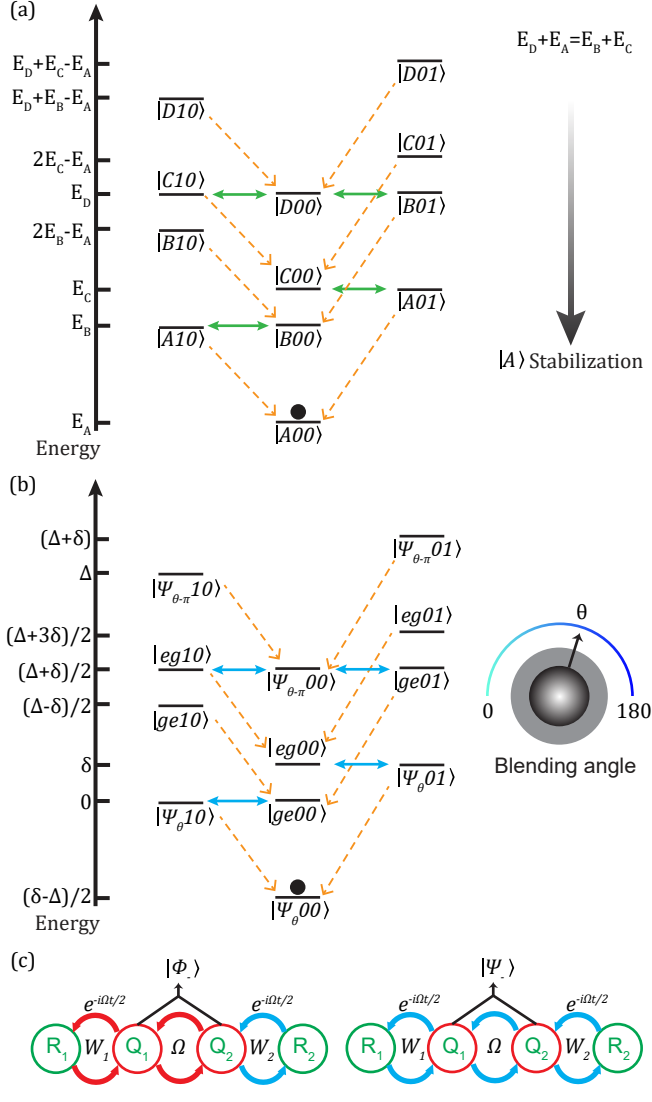
FIG. 1. (a) General stabilization scheme. Two qubits' eigenstates $\{|A\rangle, |B\rangle, |C\rangle, |D\rangle\}$ are plotted in the energy level diagram. When the energy relation $E_D + E_A = E_B + E_C$ is satisfied, $|A\rangle$ is stabilized. Qubit-resonator interactions and resonator photon decay rate κ are shown in blue and orange arrows. Qubit decay rate γ is assumed slowest and not plotted. (b) Stabilization of entangled states $|\Psi_\theta\rangle = \sin(\theta/2)|gg\rangle - \cos(\theta/2)|ee\rangle$ or $|\Phi_\theta\rangle = \sin(\theta/2)|ge\rangle - \cos(\theta/2)|eg\rangle$. (c) A special case of (b) that stabilizes the odd and even parity bell states $|\Phi_-\rangle$ and $|\Psi_-\rangle$. Circulating arrows are color-coded to represent red (exchange-like) and blue (two-photon-pumping) sidebands respectively. The QQ and QR sideband rates are separate Ω and W_j, and the QR sideband is detuned in frequency by $\Omega/2$.

two-qubit interaction H_{QQ} and qubit-resonator interactions $H_{QRj}, j = \{1, 2\}$ acting as perturbations. We label the four eigenstates of H_{QQ} as $\{|A\rangle, |B\rangle, |C\rangle, |D\rangle\}$ with eigenenergies $\{E_A < E_B \leq E_C \leq E_D\}$ so that $|A\rangle$ is the target state to stabilize. Our stabilization scheme involves engineering a one-way flow of population to $|A\rangle$

connecting all intermediate eigenstates of the system.

We now derive the energy matching requirements for an efficient stabilization protocol in our two-qubit-two-resonator system depicted in Figure 1(a). We control the form of the target stabilized state $|A\rangle$ by choosing different two-qubit interaction strengths and detunings that control H_{QQ}. We change the resonator photon energy in the rotating frame by detuning the QR interactions. The dynamics of H_{sys} are captured by considering the following set of eigenstates: $\{|A\rangle, |B\rangle, |C\rangle, |D\rangle\} \otimes \{|00\rangle, |10\rangle, |01\rangle\}$. We neglect the resonator state $|11\rangle$ as the probability of simultaneous population in both resonators $\{R_1, R_2\}$ is extremely low when resonator decay rate κ is much larger than the qubit decay rate γ (assumed identical). The central column in Fig. 1(a) shows the eigenstates of H_{QQ} with no photons in the resonators. The left column represents the same states with one photon in the left (R_1) resonator and similarly for the right column is associated with the second resonator (R_2). We engineer the photon energies in R_1 and R_2 to be $E_B - E_A$ and $E_C - E_A$ respectively through tuning the QR interactions H_{QRj}. This condition puts two transitions $|A01\rangle \leftrightarrow |C00\rangle$ and $|A10\rangle \leftrightarrow |B00\rangle$ on resonance, shown in Fig. 1(a). If $\langle A01| H_{QR1} |C00\rangle$ and $\langle A10| H_{QR2} |B00\rangle$ are non-zero, two on-resonance oscillations between $|C00\rangle$, $|A01\rangle$ and between $|A10\rangle$, $|B00\rangle$ will be created. Since both resonators are lossy, the oscillation will quickly damp to $|A00\rangle$. To complete the downward stabilization path, we need to also connect $|D00\rangle$ into the flow. We further require that the following terms are non-zero so that the transfer path is not blocked: $\langle B01| H_{QR1} |D00\rangle$, $\langle C10| H_{QR2} |D00\rangle$. If all four interaction strengths (shown in green double-headed arrows in Fig. 1(a)) are dominant over the qubit decay rate, populations in $|B\rangle$, $|C\rangle$, and $|D\rangle$ will flow to $|A\rangle$. From Fermi's golden rule, the interaction strength between two states is quadratically suppressed by their energy gap and maximized when on-resonance [24]. This imposes a simple energy-matching requirement for efficient stabilization: $E_D + E_A = E_B + E_C$. Energy degeneracy within $\{|B\rangle, |C\rangle, |D\rangle\}$ will not affect the stabilization scheme, because it will not block the dissipative flow to $|A00\rangle$ in Fig. 1(a).

As an explicit demonstration, we first stabilize a continuous set of entangled states $|\Psi_\theta\rangle = \sin(\theta/2)|gg\rangle - \cos(\theta/2)|ee\rangle$, illustrated in Fig. 1(b). Here, θ can be regarded as a "blending angle" between the two even parity states $|gg\rangle$ and $|ee\rangle$. We introduce three sideband transitions into the system: qubit-qubit (QQ) blue sideband $|gg\rangle \leftrightarrow |ee\rangle$ with rate Ω and two qubit-resonator (QR) blue sidebands $|g0\rangle \leftrightarrow |e1\rangle$ between Q_j and R_j with rate W_j. To ensure that H_{QRj} act as perturbations over H_{QQ}, we adjust the drive strengths to satisfy $\Omega \gg W_j$. We further detune the QQ, QR1, and QR2 blue sideband by δ, $(\Delta - \delta)/2$, and $(\Delta + \delta)/2$ in frequencies, with $\Delta = \sqrt{\Omega^2 + \delta^2}$. The detuning δ determines the blending angle $\theta = \tan^{-1}\left(\frac{\delta + \Delta}{\Omega}\right)$ with a range of $[0, \frac{\pi}{2})$. In the presence of these three drives, the rotating frame
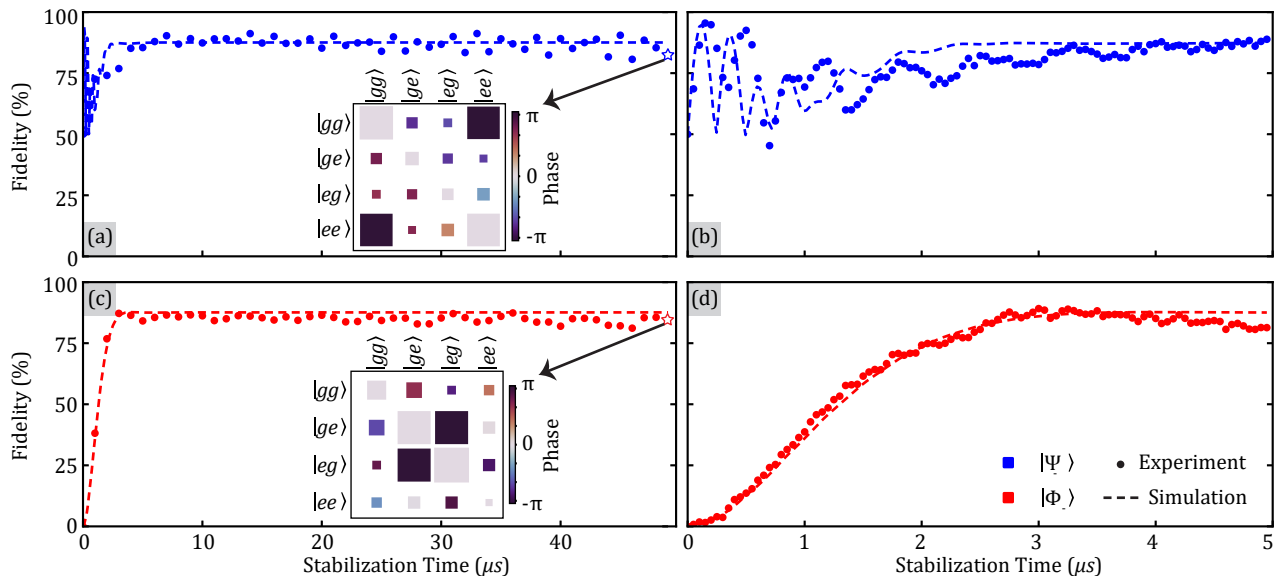
FIG. 2. Experimental demonstration of $|\Psi_-\rangle$ ((a), (b)) and $|\Phi_-\rangle$ ((c), (d)) stabilization with the initial state $|gg\rangle$. Two-qubit state tomography is performed at each time point, and the reconstructed density matrix is used to calculate the target state fidelity. The density matrices reconstructed with 5000 single shot measurements at 49 μs are plotted. Lab frame simulation results are shown in dash lines, which matched well in both short and long time scales. Parameters used in simulation: $\{\Omega, W_1, W_2, \Gamma_1, \Gamma_2\}/2\pi = \{2.0, 0.47, 0.47, 0.33, 0.43\}$ MHz for $|\Psi_-\rangle$ and $\{3.0, 0.36, 0.36, 0.33, 0.43\}$ MHz for $|\Phi_-\rangle$. Qubit coherence time is chosen as $\{T_1^{q1}, T_1^{q2}, T_\phi^{q1}, T_\phi^{q2}\} = \{25, 12, 25, 25\}$ μs.

Hamiltonian H_{sys} is

$$H_{\text{sys}} = \frac{\Omega}{2}\left(a_{q1}a_{q2} + h.c.\right) + \delta a_{q1}^\dagger a_{q1}$$
$$+ \frac{W_1}{2}\left(a_{q1}a_{r1} + h.c.\right) + \frac{W_2}{2}\left(a_{q2}a_{r2} + h.c.\right)$$
$$+ \frac{\Delta + \delta}{2}a_{r1}^\dagger a_{r1} + \frac{\Delta - \delta}{2}a_{r2}^\dagger a_{r2}. \tag{1}$$

Here a_{qj} and a_{rj} are separately the j-th qubit's and resonator's annihilation operator. Under the combined conditions $\Omega \gg W_j \sim \kappa \gg \gamma$ and $W_j = W$, the eigenstates with zero resonator photons are $\{|\Psi_\theta 00\rangle, |ge00\rangle, |eg00\rangle, |\Psi_{\pi-\theta}00\rangle\}$, with corresponding eigenenergies $\{(\delta - \Delta)/2, 0, \delta, (\delta + \Delta)/2\}$. Assuming the lossy resonator has a Lorentzian energy spectrum, the two-step refilling rate Γ_t from $|eg00\rangle$ to $|\Psi_\theta 00\rangle$ ($|eg00\rangle \leftrightarrow |\Psi_\theta 01\rangle$, $|\Psi_\theta 01\rangle \rightarrow |\Psi_\theta 00\rangle$) is [24]

$$\Gamma_t = \frac{W^2 \cos^2(\theta/2)\,\kappa}{\kappa^2 + W^2 \cos^2(\theta/2)}. \tag{2}$$

The other two-step transitions $|ge00\rangle \rightarrow |\Psi_\theta 00\rangle$, $|\Psi_{\theta-\pi}00\rangle \rightarrow |ge00\rangle$, and $|\Psi_{\theta-\pi}00\rangle \rightarrow |eg00\rangle$ also have the same rate. Therefore, the steady-state fidelity $\mathcal{F}_\infty$ for $|\Psi_\theta 00\rangle$ is (ignoring all off-resonant transitions, see Appendix. B for detail)

$$\mathcal{F}_\infty = \left(\frac{\Gamma_t + \gamma \sin^2(\theta/2)}{\Gamma_t + \gamma}\right)^2. \tag{3}$$

Similarly, we can stabilize another set of entangled states with odd parity $|\Phi_\theta\rangle = \sin(\theta/2)|ge\rangle -$

$\cos(\theta/2)|eg\rangle$. We introduce three sideband interactions: QQ red $|eg\rangle \leftrightarrow |ge\rangle$, QR1 red $|e0\rangle \leftrightarrow |g1\rangle$, and QR2 blue $|g0\rangle \leftrightarrow |e1\rangle$ with rates $\{\Omega, W_3, W_4\}$ and frequency detunings $\{\delta, (\Delta + \delta)/2, (\Delta - \delta)/2\}$ respectively. Under this condition, four resonant interactions will appear: $|gg00\rangle \leftrightarrow |\Phi_\theta 01\rangle$, $|ee00\rangle \leftrightarrow |\Phi_\theta 10\rangle$, $|ee01\rangle \leftrightarrow |\Phi_{\theta-\pi}00\rangle$, and $|gg10\rangle \leftrightarrow |\Phi_{\theta-\pi}00\rangle$. The detuning similarly sets the blending angle $\theta = \arctan\left(\frac{\delta+\Delta}{\Omega}\right)$.

With the above construction, we create a stabilization protocol that can freely tune the blending angles. As a special case, when QQ sideband detuning ($\delta = 0$), the blending angle for both cases is $\theta = \frac{\pi}{2}$, which corresponds to the odd and even parity Bell states $|\Phi_-\rangle = (|ge\rangle - |eg\rangle)/\sqrt{2}$ and $|\Psi_-\rangle = (|gg\rangle - |ee\rangle)/\sqrt{2}$, shown in Fig. 1(c).

In fact, this stabilization protocol can be generalized to stabilize an even larger group of states, including both entangled and product states, as long as the energy matching requirement $E_D + E_A = E_B + E_C$ is satisfied when engineering H_{QQ}. The following is a list of tunable parameters to engineer H_{QQ}: QQ sideband strength Ω, QQ sideband detunings δ, single qubit Rabi drive strength, and single qubit Rabi drive detunings. Corresponding stabilized state $|A\rangle$ is determined from H_{QQ}. Details about the stabilizable manifold are discussed in Appendix. D.

III. EXPERIMENTAL RESULTS

We perform the stabilization experiment in a system with two transmons capacitively coupled to two lossy
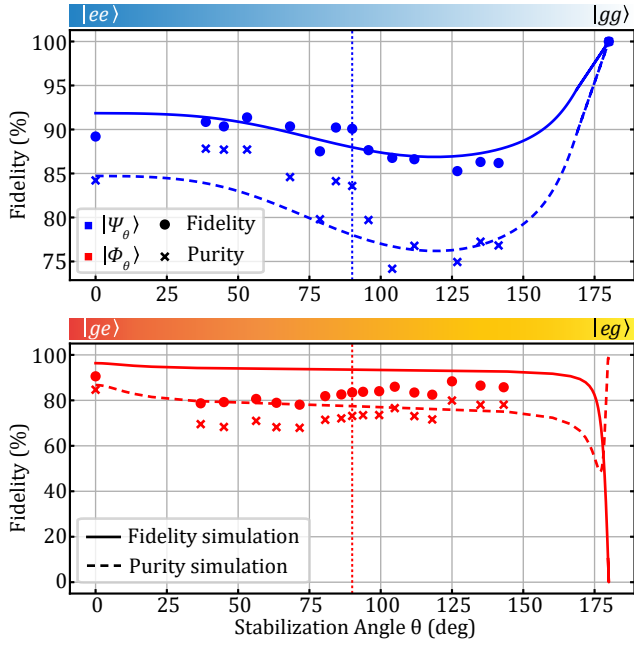
FIG. 3. Spectroscopy of universal Bell-state stabilization. $|\Psi_\theta\rangle$ (top) and $|\Phi_\theta\rangle$ (bottom) are separately stabilized with a measured fidelity above 78% among different blending angle θ. The fidelities are measured after 40 μs of stabilization. For stabilizing $|gg\rangle$, no external drives are applied. For $|\Phi_\theta\rangle$ case, the fidelity dropped to 0 near $\theta = \pi$. The dotted lines indicate simulated fidelities for the odd and even parity Bell state stabilization. All parameters used in the simulation are the same as in Fig. 2.

resonators (See Appendix. A). Two transmons are inductively coupled through a SQUID loop. All QQ sidebands and QR red sidebands are realized through modulating the SQUID flux at corresponding transition frequencies. QR blue sidebands are achieved by sending a charge drive to the transmon at half the transition frequencies. The experimentally measured qubit coherence are $T_1 = 24.3\,\mu s$ (9.1 μs), $T_{\rm Ram} = 15.2\,\mu s$ (9.8 μs), $T_{\rm echo} = 24.6\,\mu s$ (14.3 μs) for $Q_1(Q_2)$, and the measured resonator decay rate $\kappa/2\pi$ are $\{0.33, 0.43\}$ MHz for R_1 and R_2 respectively.

Figure 2 shows the time evolution of state fidelity for the odd and even parity Bell state stabilization. To stabilize $|\Psi_-\rangle$, a $\Omega = 2\pi \times 2.0$ MHz QQ blue sideband, $W_1 = W_2 = 2\pi \times 0.47$ MHz QR blue sidebands are simultaneously applied to the system. Both QR sidebands are detuned by $\Omega/2 = 2\pi \times 1.0$ MHz in frequency to implement the stabilization scheme depicted in Fig. 1(c). For each stabilization experiment, we reconstruct the system density matrix through two-qubit state tomography using 5000 repetitions of 9 different prerotations. The stabilization fidelity measured at 49 μs (much longer than single qubit T_1 and $T_{\rm Ram}$) is 82.5%. To stabilize $|\Phi_-\rangle$, a $\Omega = 2\pi \times 3.0$ MHz QQ red sideband, $W_1 = W_2 = 2\pi \times 0.36$ MHz QR1 red and QR2 blue sidebands are simultaneously applied to the system, with

both QR sidebands detuned by $\Omega/2 = 2\pi \times 1.5$ MHz. The stabilization fidelity measured at 49 μs is 84.6%. The two-qubit state tomography data at 49 μs after ZZ coupling correction [25] are shown for both stabilization cases.

Next, we introduce QQ sideband detunings δ and stabilize more general entangled states $|\Psi_\theta\rangle$ and $|\Phi_\theta\rangle$. We choose the same sideband strengths ($\{\Omega, W_1, W_2\}/2\pi = \{2.0, 0.47, 0.47\}(\{3.0, 0.36, 0.36\})$ MHz for $|\Psi_\theta\rangle(|\Phi_\theta\rangle)$ case) and detune QR sideband frequencies accordingly to maximize the stabilization fidelity measured at 40 μs. The experimentally measured state fidelity and state purity as a function of θ are shown in Fig. 3. Under the current QR sideband color combination, $|\Phi_\theta\rangle$ fails to stabilize near $\theta = 180°$. This is because the interaction strength $\langle gg00|H_{\rm sys}|\Phi_\theta 01\rangle$ and $\langle ee00|H_{\rm sys}|\Phi_\theta 10\rangle$ are close to 0. Swapping QR1 and QR2 sidebands' color and detuning performs a transformation $\theta \to \theta - \pi$ in the stabilized state. This ensures a high stabilization fidelity for arbitrary stabilization angles. Details about changing sideband colors and detunings to ensure high fidelity are presented in Appendix. E

The flexibility in our schemes and easy access to different sidebands in our device allow a further demonstration — fast dissipative switching between stabilized states. Here, we implement such an operation that can flip the parity of the stabilized Bell pair by changing sideband combinations, shown in Fig. 1. To quantify the stabilized parity, we measure the system's density matrix ρ and define the parity signature as $2(|\langle ee|\rho|gg\rangle| - |\langle ge|\rho|eg\rangle|)$ describing the difference in relevant coherence parameters. The results are shown in Fig. 4. The scaling factor is chosen such that the ideal even and odd Bell pairs have parity signatures of ± 1. Starting from the ground state $|Q_1 Q_2\rangle = |gg\rangle$, the stabilized state is set to even parity Bell pair $(|gg\rangle - |ee\rangle)/\sqrt{2}$, and we switch the parity every 20 μs. At 20 μs, the stabilized state is switched to odd parity Bell pair $(|ge\rangle - |eg\rangle)/\sqrt{2}$, and stabilization happens quickly with a time constant $\tau_r = 1.80\,\mu s$. At 40 μs, the switching from odd to even parity results in a faster stabilization with $\tau_b = 0.91\,\mu s$. The switching at 60 μs to odd Bell state shows a similar τ_r of 2.20 μs. We leave the stabilization drives turned on for another 25 μs to prove that the performance is not degraded after a few switching operations.

Further improvement of the stabilized state's fidelity is possible by reducing the transition ratio $\frac{\gamma}{\Gamma_t}$ (from Eq. 3) and increasing QQ sideband rate Ω for a larger energy gap. Increasing qubit dephasing time also improves stabilization fidelity (discussed in the Appendix. C). To speed up the stabilization, i.e., reduce time constants, we need to increase the refilling rate Γ_t. Since QR sideband rate W is bounded by the QQ sideband rate Ω to ensure the validity of the perturbative approximation, given a fixed W, Γ_t is maximized when the resonator decay rate $\kappa = W\cos(\theta/2)$. For the even and odd parity Bell states, further increase in both resonators' κ compared to our current parameters would thus be beneficial. More details about stabilization robustness are discussed in Ap-
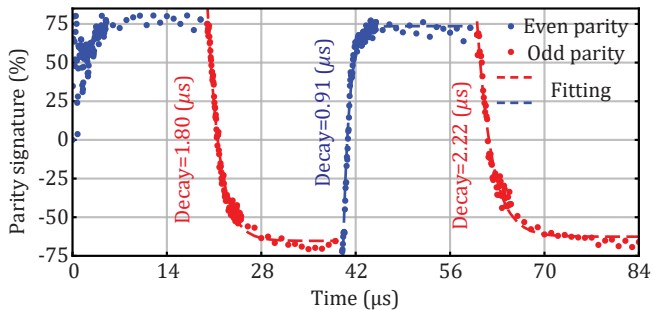
FIG. 4. Dissipative switching of Bell state parity. The initial state is $|gg\rangle$, and the switch status is set to even parity between $[0\,\mu s, 20\,\mu s]$ and $[40\,\mu s, 60\,\mu s]$, and to odd parity between $[20\,\mu s, 40\,\mu s]$ and $[60\,\mu s, 85\,\mu s]$. Each experimental point is measured with the two-qubit state tomography. Stabilization time is calculated by fitting the parity signature to exponential decay after each switching event.

pendix. C. To stabilize a more general set of states shown in Appendix. D, longer qubit coherence is needed to improve the experimental resolution between different stabilized states in this manifold and is a subject of future work.

IV. CONCLUSION

In conclusion, we demonstrate a two-qubit programmable stabilization scheme that can autonomously stabilize a continuous set of entangled states. We develop an inductively coupled two-qubit device that provides access to both QQ and QR sideband interactions required. The stabilization fidelity among all stabilization angles is above 78%, specifically, we achieved high Bell pair stabilization fidelity (84.6% for the odd parity and 82.5% for the even parity) as two special points. We further demonstrate a parity switching capability between the Bell pairs with fast stabilization time constants ($< 2\ \mu s$). We believe such freedom in choosing stabilized states will inspire generalization to autonomous stabilization of larger systems, large-scale many-body entanglement [3], remote entanglement [26], density matrix exponentiation [20, 21], and new AQEC logical codewords in the future.

V. ACKNOWLEDGMENT

Appendix A: Device Hamiltonian and realized sidebands

Figure 5 shows the inductively coupled two-qubit device used in the stabilization demonstration. Two transmon qubits (red) share a common ground, which is interrupted by a SQUID (purple). Each transmon is capacitively coupled to a lossy resonator (green) also serving as the dispersive readout.

The flux line near the SQUID provides a continuous DC bias $\varphi_{\mathrm{dc}} = 0.3795\pi$ in our experiment. The measured qubit coherence and frequencies at this flux point are shown in Table. I. By sending RF flux drives at appropriate frequencies through the flux line, the inductive coupler can provide either QQ red sideband or QQ blue sideband. The Hamiltonian for qubits and coupler is shown in Eq. A1a. For a detailed description on the adiabatic approximation of the inductive coupler, we draw the attention of the readers to the references 12 and 8. Following is a summary. The Hamiltonian of the circuit

$\varphi_{\mathrm{dc}} = 0.0$	$T_1(\mu s)$	$T_{\mathrm{Ram}}(\mu s)$	$T_{\mathrm{echo}}(\mu s)$
Q_1	31.6	28.4	26.6
Q_2	2.8	4.9	

$\varphi_{\mathrm{dc}} = 0.3795\pi$	$T_1(\mu s)$	$T_{\mathrm{Ram}}(\mu s)$	$T_{\mathrm{echo}}(\mu s)$
Q_1	24.3	15.2	24.6
Q_2	9.1	9.8	14.3
R_1	0.48		
R_2	0.37		

Parameter	Symbol	Value/2π
Q_1 ge frequency	$\omega_{q1}/2\pi$	3.2046 (GHz)
Q_2 ge frequency	$\omega_{q2}/2\pi$	3.6624 (GHz)
Q_1 anharmonicity	$\alpha_1/2\pi$	-116.3 (MHz)
Q_2 anharmonicity	$\alpha_2/2\pi$	-159.5 (MHz)
Readout1 frequency	$\omega_{r1}/2\pi$	4.9946 (GHz)
Readout2 frequency	$\omega_{r2}/2\pi$	5.4505 (GHz)
$\left(E_{|ee\rangle} - E_{|ge\rangle}\right) - \left(E_{|eg\rangle} - E_{|gg\rangle}\right)$	$ZZ/2\pi$	-261 (kHz)
Readout1 fidelity		88.87%
Readout2 fidelity		81.76%

TABLE I. Device coherence and frequencies at the coupler biasing point $\varphi_{\mathrm{dc}} = 0.3795\pi$ (top and middle), and the coherence at the coupler sweet spot $\Phi_{\mathrm{dc}} = 0\pi$ (bottom). Q_2 experiences higher loss at the sweet spot from a near two-level system. At the sweet spot, Q_1's decoherence and echo time are similar to those at our experiment's biasing point.
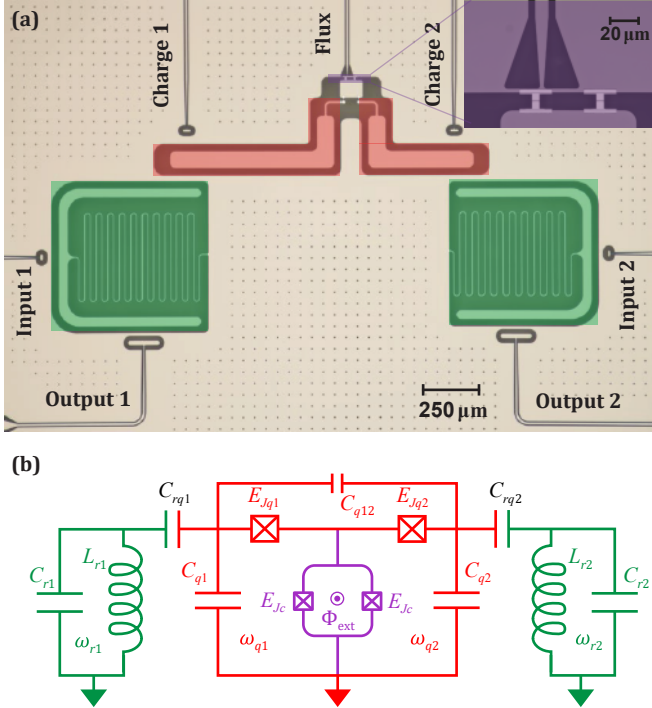

FIG. 5. The device. (a) False-colored optical image of the device. The inset shows a zoomed-in image of the inductive coupler. (b) Circuit diagram of the device. Coupler junctions' intrinsic capacitance C_{qc} is included in the quantization analysis.

containing two qubits and the coupler is described by

$$H = \overrightarrow{n}^{\mathsf{T}} C_L^{-1} \overrightarrow{n} - E_{j1} \cos\left(\phi_c - \phi_1\right) - E_{j2} \cos\left(\phi_2 - \phi_c\right),$$
$$- E_{jc} \cos\left(\frac{\Phi_{\mathrm{ext}}}{\Phi_0}\right) \cos\left(\phi_c\right), \tag{A1a}$$

$$C_L = \begin{bmatrix} C_{q1} + C_{q12} & -C_{q12} & 0 \\ -C_{q12} & C_{q2} + C_{q12} & 0 \\ 0 & 0 & C_{q1} + C_{q2} + C_{qc} \end{bmatrix} \tag{A1b}$$

$$\overrightarrow{n}^{\mathsf{T}} = (n_1, n_2, n_c).$$

Here, phase variables $\phi_{1,2,c}$, charge variables $n_{1,2,c}$, and Josephson energy $E_{j1,j2,jc}$ are for qubit 1, qubit 2, and the coupler, and C_{qc} is the intrinsic capacitance from the coupler junction. After quantization, one can arrive at the following:

$$H_{ab} = \omega_{q1} a_{q1}^\dagger a_{q1} + \omega_{q2} a_{q2}^\dagger a_{q2}$$
$$+ \frac{\alpha_1}{2} a_{q1}^\dagger a_{q1}^\dagger a_{q1} a_{q1} + \frac{\alpha_2}{2} a_{q2}^\dagger a_{q2}^\dagger a_{q2} a_{q2}$$
$$+ g_1(t)\left(a_{q1}^\dagger + a_{q1}\right)\left(a_{q2}^\dagger + a_{q2}\right)$$
$$+ g_2\left(-a_{q1}^\dagger + a_{q1}\right)\left(-a_{q2}^\dagger + a_{q2}\right), \tag{A2a}$$

$$g_1(t) = \frac{\sqrt{E_{j1}E_{j2}}}{2E_{jc}\cos\left(\frac{\Phi_{\mathrm{ext}}(t)}{\Phi_0}\right)}\sqrt{\omega_{q1}\omega_{q2}}, \tag{A2b}$$

$$g_2 = \frac{\sqrt{C_{q1}C_{q2}}}{2C_{q12}}\sqrt{\omega_{q1}\omega_{q2}}. \tag{A2c}$$
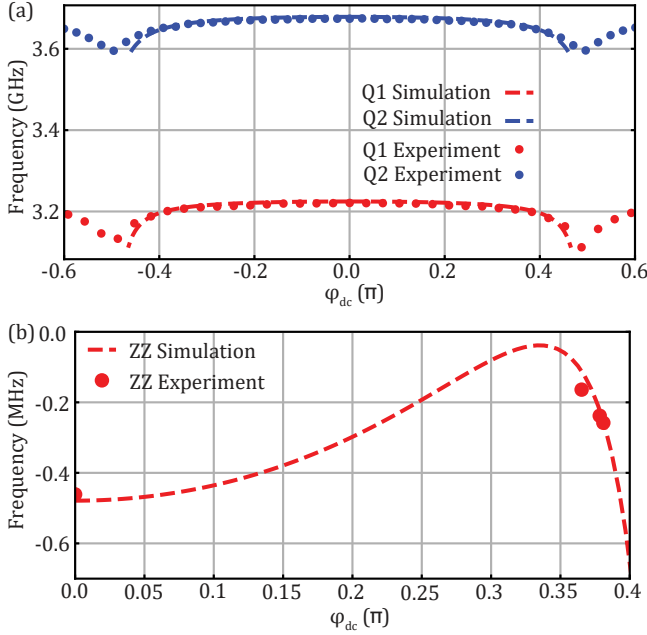
FIG. 6. Coupler DC flux sweep of (a) qubits frequencies and (b) ZZ coupling strength between qubits. Circuit quantization results and experimentally measured data are separately shown in dash lines and dots.

In the experiment, we have $E_{jc} = 1700\,\text{GHz} \gg E_{j1}(E_{j2}) = 12.2\,\text{GHz}(12.3\,\text{GHz})$, making the coupler mode much heavier than the qubit modes. This strong asymmetry enables the adiabatic removal of the coupler dynamics: We treat the coupler as a linear inductance and assume the coupler mode is static. By removing the linear mode through minimizing the system energy, we arrive at the approximated Hamiltonian in Eq. A2a. When modulating the external RF flux threaded the coupler, the transverse coupling strength $g_1(t)$ will also be modulated accordingly. By plugging the RF flux modulation $\Phi_{\text{ext}}/\Phi_0 = \varphi_{\text{dc}} + \epsilon\cos(\omega_d t)$ into Eq. A2b and assuming the flux modulation ϵ is much smaller than Φ_{dc}, we have:

$$
\begin{aligned}
g_1(t) &= \frac{\sqrt{E_{j1}E_{j2}}}{2E_{jc}}\sqrt{\omega_{q1}\omega_{q2}}\frac{1}{\cos(\varphi_{\text{dc}} + \epsilon\cos(\omega_d t))} \\
&\approx \frac{\sqrt{E_{j1}E_{j2}}}{2E_{jc}}\sqrt{\omega_{q1}\omega_{q2}}\frac{(1 + \epsilon\sin(\omega_d t)\tan(\varphi_{\text{dc}}))}{\cos(\varphi_{\text{dc}})}
\end{aligned}
\tag{A3a}
$$

Therefore the QQ sideband rate is roughly $\epsilon\frac{\sqrt{E_{j1}E_{j2}}}{2E_{jc}}\sqrt{\omega_{q1}\omega_{q2}}\frac{\tan(\varphi_{\text{dc}})}{\cos(\varphi_{\text{dc}})}$, which is proportional to the flux modulation rate and increases with φ_{dc}. We choose $\varphi_{\text{dc}} = 0.3795\pi$ based on qubit coherence, sideband rate, and small ZZ coupling between qubits. When the resonator is capacitively coupled to the qubit at strength g_{qr} and frequency difference Δ, the QR sideband can also be modulated through the flux line, and the sideband rate is multiplied by an extra mode dressing coefficient $\frac{g_{qr}}{\Delta}$. By changing the RF modulation
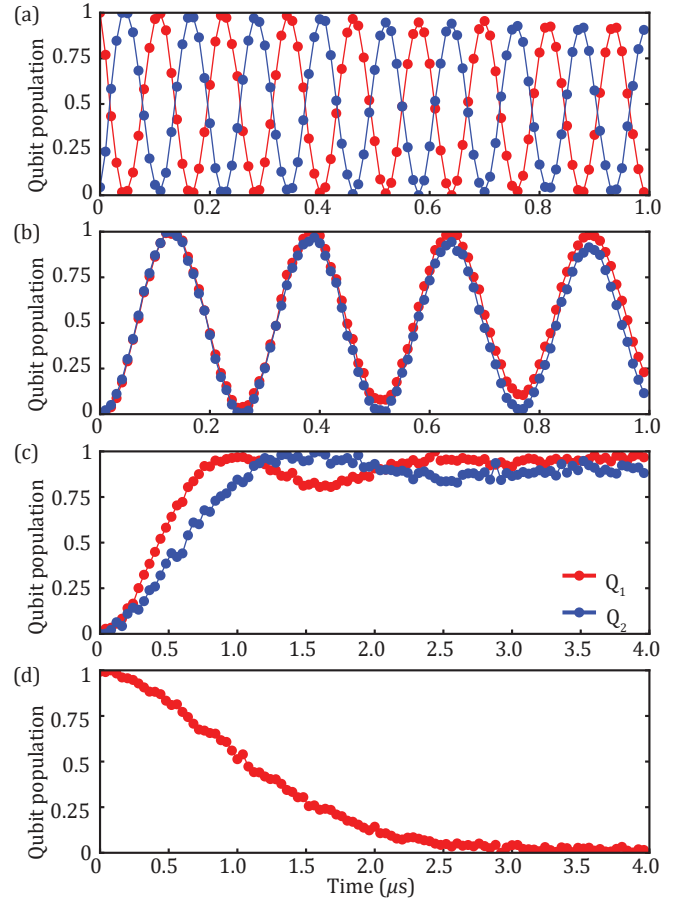

FIG. 7. Experimentally realized QQ and QR sidebands. From top to bottom are separately (a) QQ red sideband $|ge\rangle \leftrightarrow |eg\rangle$, (b) QQ blue sideband $|gg\rangle \leftrightarrow |ee\rangle$, (c) QR blue sideband between QR1 and QR2 $|g0\rangle \leftrightarrow |e1\rangle$, and (d) QR1 red sideband $|e0\rangle \leftrightarrow |g1\rangle$. Readout on Q_1 (red) and Q_2 (blue) are scaled between 0 ($|g\rangle$) and 1 ($|e\rangle$). Data points are connected for visual guidance.

frequency ω_d, we can activate different colors of QQ and QR sidebands.

Both QQ red, QQ blue, and QR red sidebands are generated through flux modulation at a decent rate. The QR blue sidebands have a different choice to activate [27]: The direct charge drives at half of the transition frequency with amplitude ϵ_q can provide an effective rate of $W = 16g_{qr}^3\epsilon_q^2/\Delta^4$. This turned out to be easier to realize with our device, and we achieve at least 0.5 MHz QR blue sideband rate.

Figure 7 demonstrates all realized QQ and QR sidebands needed for the stabilization experiments. Fast QQ red sidebands at 8.5 MHz and modest QQ blue sidebands at 3.9 MHz are performed in the experiment through RF flux modulation of the inductive coupler. Both readouts for QQ red sideband (with initial state $|eg\rangle$) and QQ blue sideband (with initial state $|gg\rangle$) are shown in Fig. 7(a) and (b). The QR blue sidebands are generated through the charge lines that are coupled to the qubit pads, shown

in Fig. 7(c) with initial state $|g0\rangle$. The QR1 red side-bands are activated through the coupler flux modulation. The on-resonance readout trace for Q_1 starting at $|e0\rangle$ is plotted in Fig. 7(d).

Appendix B: Derivation of steady-state fidelity

We take the stabilization of $|\Psi_\theta\rangle = \sin(\theta/2)|gg\rangle - \cos(\theta/2)|ee\rangle$ as an example to compute the steady-state fidelity in detail. Suppose the steady state population at the four basis states $\{|\Psi_\theta\rangle, |ge\rangle, |eg\rangle, |\Psi_{\theta-\pi}\rangle\}$ are separately $\{w, x, y, z\}$. We assume the photon population in both resonators are transitional and ignore their contribution to the steady-state fidelity. This means $w + x + y + z = 1$. The steady-state configuration should balance the following two processes:

(a) two-step refilling process: $|ge\rangle \rightarrow |\Psi_\theta\rangle$, $|eg\rangle \rightarrow |\Psi_\theta\rangle$, $|ge\rangle \rightarrow |\Psi_\theta\rangle$, and $|ge\rangle \rightarrow |\Psi_\theta\rangle$. All the transition rates are the same

$$\Gamma_t = \frac{W^2 \cos^2(\theta/2)\kappa}{\kappa^2 + W^2 \cos^2(\theta/2)} \tag{B1}$$

(b) Single photon loss in each qubit. The following four transitions have the same rate $\sin^2(\theta/2)\gamma$: $|ge\rangle \rightarrow |\Psi_\theta\rangle$, $|eg\rangle \rightarrow |\Psi_\theta\rangle$, $|ge\rangle \rightarrow |\Psi_{\theta-\pi}\rangle$, and $|eg\rangle \rightarrow |\Psi_{\theta-\pi}\rangle$. The reversed four transitions have the same rate $\cos^2(\theta/2)\gamma$.

Therefore, the steady-state population should satisfy the following equations

$$\begin{cases} (\Gamma_t + \sin^2(\theta/2)\gamma)(x+y) - 2\cos^2(\theta/2)\gamma w & = 0, \\ (\Gamma_t + \sin^2(\theta/2)\gamma)z + \cos^2(\theta/2)\gamma w - (\Gamma_t + \gamma)x & = 0, \\ (\Gamma_t + \sin^2(\theta/2)\gamma)z + \cos^2(\theta/2)\gamma w - (\Gamma_t + \gamma)y & = 0, \\ 2\cos^2(\theta/2)\gamma(x+y) - (2\Gamma_t + 2\sin^2(\theta/2)\gamma)z & = 0, \\ w + x + y + z & = 1. \end{cases} \tag{B2}$$

This gives the following populations

$$\begin{cases} w & = \left(\frac{\Gamma_t + \gamma\sin^2(\theta/2)}{\Gamma_t + \gamma}\right)^2, \\ x & = \frac{\cos^2(\theta/2)\gamma}{\Gamma_t + \gamma - \cos^2(\theta/2)\gamma}w, \\ y & = x, \\ z & = \frac{\cos^2(\theta/2)\gamma}{\Gamma_t + \sin^2(\theta/2)\gamma}x. \end{cases} \tag{B3}$$

And $w = \mathcal{F}_\infty$ is the steady state fidelity.

Appendix C: Stabilization robustness

We study the stabilization robustness for $|\Psi_-\rangle$ and $|\Phi_-\rangle$ in this section. For other stabilization angles, the discussion is similar. Figure 8 shows the rotating frame simulation of steady-state fidelity by sweeping different stabilization parameters. For the $|\Psi_-\rangle$ case, the Hamiltonian used in the simulation is Eq. 1, and for the $|\Phi_-\rangle$ case the Hamiltonian is modified accordingly with a different sideband combinations (See Fig. 1(c)). We study
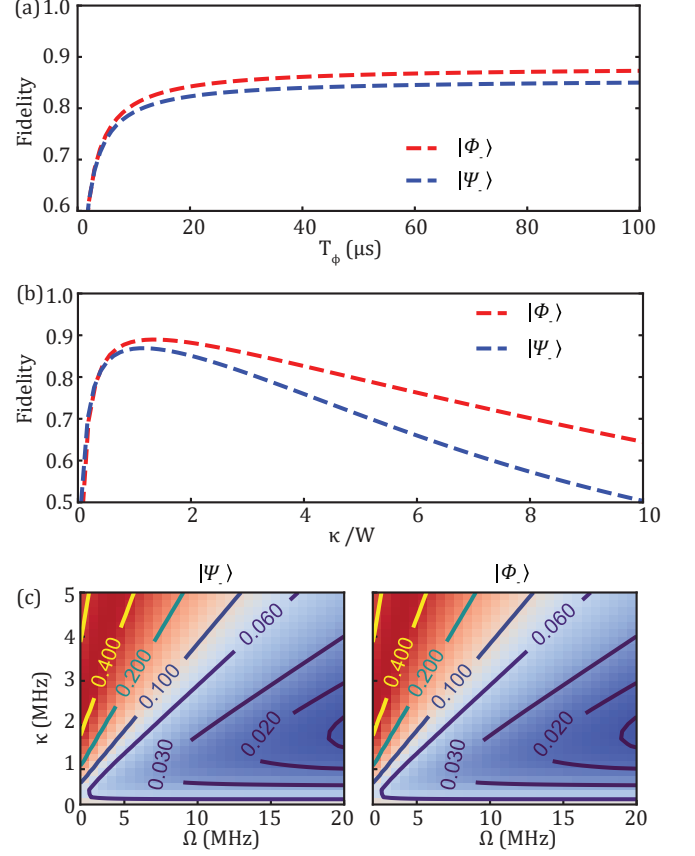

FIG. 8. Rotating frame simulation of even and odd parity bell states' stabilization fidelity: (a) Sweeping qubit dephasing time. The other simulation parameters are the same as the experiments. (b) Sweeping the ratio between resonator decay rate κ and QR sideband strength W without qubit dephasing. (c) 2D sweep of κ and QQ sideband strength Ω without qubit dephasing, setting $W = \kappa$. Infidelities are shown on the contours.

the state fidelity by varying parameters step-by-step towards the ideal case. First, we show that longer qubit dephasing time helps improve steady-state fidelity. In Fig. 8 (a), we sweep qubit's dephasing time (assuming the same for both qubits) while choosing the following parameters $\{\Omega, \frac{W_1}{2}, \frac{W_2}{2}, \Gamma_1, \Gamma_2\}/2\pi$ in the simulation

$$|\Psi_-\rangle \text{ case} : \{1.4, 0.35, 0.35, 0.30, 0.33\}\text{MHz},$$
$$|\Phi_-\rangle \text{ case} : \{3.0, 0.32, 0.32, 0.30, 0.33\}\text{MHz}.$$

We set the following qubit decoherence time $\{T_1^{q1}, T_1^{q2}\} = \{21, 9\}\mu s$. The steady state fidelities rise above 80% quickly after T_ϕ exceeds $10\,\mu s$. The fidelity for odd and even parity bell pairs saturate at 87.3% and 85.0% with the parameters used in the simulation. This demonstrates that steady-state fidelity increases as qubit dephasing time increases.

In Fig. 8(b), we ignore the qubit dephasing and only sweep resonator decay rate κ. For simplicity, we assume QR sideband rates and resonator decay rate are the same:

$W_1 = W_2 = W$ and $\kappa_1 = \kappa_2 = \kappa$. The fidelity peak for both parity pairs appears at $W = \kappa$. This can be understood as the refilling rate Γ_t (Eq. 2) achieves the maximum at this point, therefore the steady-state fidelity (Eq. 3) is also maximized at this point.

Finally, we choose the maximum refilling rate set $W = \kappa$ in Fig. 8(c) and sweep both the QQ sidebands rate Ω and resonator decay rate κ. The infidelity of the steady states is shown in contours. Larger Ω and κ suppresses the infidelity efficiently. This indicates that our steady-state fidelity in the experiment is mainly limited by the sideband strengths. By increasing the QQ sidebands rate to above $2\pi \times 10$ MHz, in simulation, it is possible to achieve stabilization fidelity above 98%.

Appendix D: Other stabilization combinations

Here we provide a list of states that can be stabilized with our protocol.

Case 1: Any two-qubit product states.

$$|\psi_{\phi_1,\phi_2}\rangle = (\cos(\phi_1/2)\,|g\rangle + \sin(\phi_1/2)\,|e\rangle)\otimes$$
$$(\cos(\phi_2/2)\,|g\rangle + \sin(\phi_2/2)\,|e\rangle). \quad (D1)$$

This can be achieved by applying two detuned single qubit rabi drives on both Q_1 and Q_2 with rate $\{A_1, A_2\}$ and detunings $\{\delta_1, \delta_2\}$. The two-qubit rotating frame Hamiltonian becomes

$$H_p = \begin{bmatrix} 0 & A_2/2 & A_1/2 & 0 \\ A_2/2 & \delta_2 & 0 & A_1/2 \\ A_1/2 & 0 & \delta_1 & A_2/2 \\ 0 & A_1/2 & A_2/2 & \delta_1 + \delta_2 \end{bmatrix}. \quad (D2)$$

$$(D3)$$

It can be easily verified that the four eigenenergies $\{E_A < E_B < E_C < E_D\}$ satisfy the requirements $E_A + E_D = E_B + E_C$. Therefore, the lowest energy eigenstate can be efficiently stabilized by detuning two QR sideband frequencies. This is also a direct extension of the single-qubit stabilization scheme [12] to the two-qubit case.

Case 2: Dressed parity Bell states. The stabilized state set can be described by one continuous variable θ_1

$$|\zeta_{\theta_1}\rangle = \cos(\theta_1/2)\,|\Psi_-\rangle + \sin(\theta_1/2)\,|\Phi_-\rangle. \quad (D4)$$

In this case, we apply on-resonant QQ blue and single qubit rabi drive on Q_1 with rate Ω and A_1 to dress the stabilized state's parity. The two-qubit Hamiltonian H_b can be written as

$$H_b = \begin{bmatrix} 0 & 0 & A_1/2 & \Omega/2 \\ 0 & 0 & 0 & A_1/2 \\ A_1/2 & 0 & 0 & 0 \\ \Omega/2 & A_1/2 & 0 & 0 \end{bmatrix}. \quad (D5)$$

One can verify that the four eigenenergies $E_A < E_B, < E_C < E_D$ of H_b satisfy the requirement $E_A + E_D = E_B +$
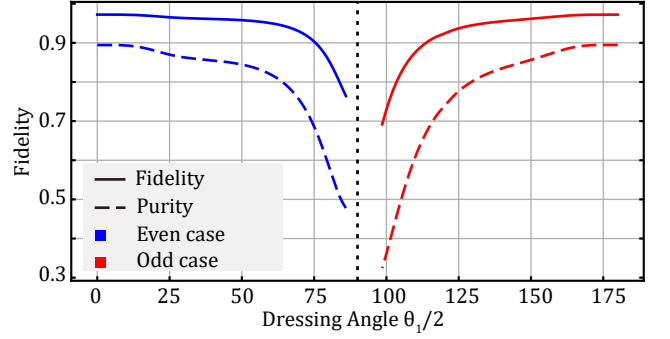

FIG. 9. Stabilizing a one-dimensional set of entangled states. Blue and red lines represent separately using the QQ blue and QQ red sideband in the rotating frame simulation. Parameter used in the simulation: $\{\Omega, W_1, W_2, \kappa_1, \kappa_2\}/2\pi = \{5.0, 0.5, 0.5, 0.3, 0.33\}$ MHz. Qubit coherence time are $\{T_1, T_\phi\} = \{30, 30\}\mu$s.

E_C. By choosing QR sidebands detunings as $E_B - E_A$ and $E_C - E_A$, the eigenstate $|A\rangle = |\zeta_{\theta_1}\rangle$ is stabilized, with the dressing angle being

$$\theta_1 = 2\arctan\left(\frac{2A_1}{\Omega + \sqrt{4A_1^2 + \Omega^2}}\right). \quad (D6)$$

Similarly, we apply on-resonant QQ red sideband and single qubit rabi drive on Q_1 with rate Ω and A_1. The two-qubit Hamiltonian H_r is

$$H_r = \begin{bmatrix} 0 & 0 & A_1/2 & 0 \\ 0 & 0 & \Omega/2 & A_1/2 \\ A_1/2 & \Omega/2 & 0 & 0 \\ 0 & A_1/2 & 0 & 0 \end{bmatrix}. \quad (D7)$$

The dressing angle θ_1 under this case is

$$\theta_1 = \pi - 2\arctan\left(\frac{2A_1}{\Omega + \sqrt{4A_1^2 + \Omega^2}}\right). \quad (D8)$$

Steady-state fidelity is calculated through Qutip simulation for both cases, shown in Fig. 9. By combining different QQ sideband colors, all dressing angles are stabilized with the scheme, except the small band region around $\theta_1 = \pi$ where the effective transition rates provided by QR sidebands are close to 0.

Case 3: Rabi-dressed entangled states. This is a more general case where a two-dimensional set of entangled states is stabilized. We simultaneously apply a single qubit rabi drive on Q_1 with the rate A_1 and detuned QQ blue sideband with rate Ω and detuning δ. The rotating frame Hamiltonian is

$$H_g = \begin{bmatrix} -\delta/2 & 0 & A_1/2 & \Omega/2 \\ 0 & \delta/2 & 0 & A_1/2 \\ A_1/2 & 0 & -\delta/2 & 0 \\ \Omega/2 & A_1/2 & 0 & \delta/2 \end{bmatrix}. \quad (D9)$$
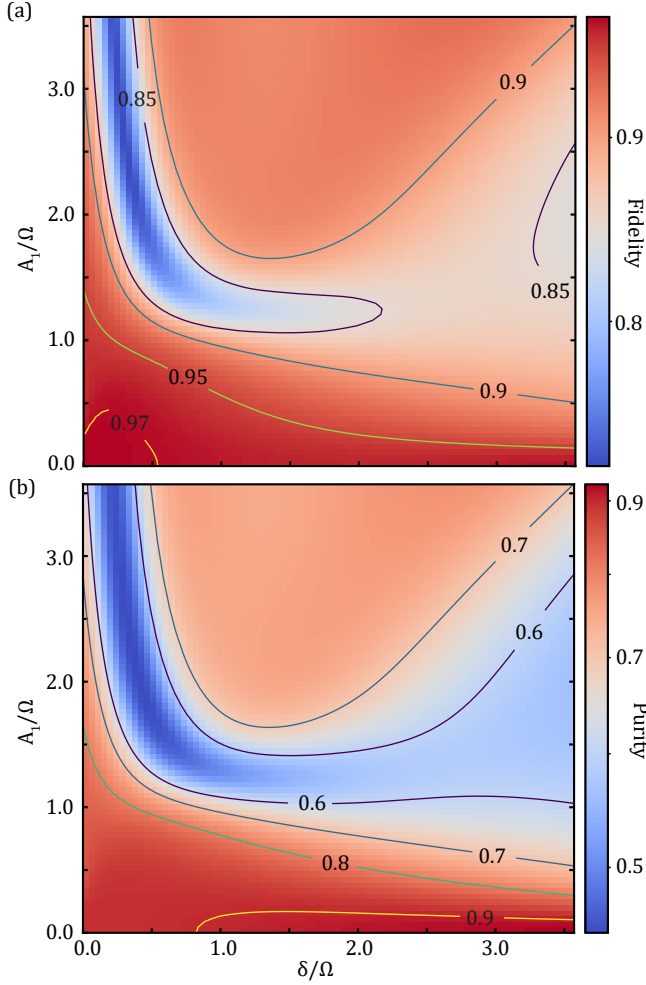
(a)

(b)

FIG. 10. Stabilizing a 2D set of entangled states. Steady states' fidelity (a) and purity (b) are simulated in the rotating frame and plotted. $\frac{A_1}{\Omega}$ and $\frac{\delta}{\Omega}$ are separately two free variables that are swept to stabilize different states. Parameter used in the simulation: $\{\Omega, W_1, W_2, \kappa_1, \kappa_2\}/2\pi = \{5.0, 0.5, 0.5, 0.3, 0.33\}$ MHz. Qubit coherence time are $\{T_1, T_\phi\} = \{30, 30\}\mu$s.

energy eigenstate is stabilized

$$
\begin{aligned}
|\xi_{\delta, A_1}\rangle =& E_{00}|gg\rangle + E_{01}|ge\rangle + E_{10}|eg\rangle - |ee\rangle, \\
x =& \sqrt{4\delta^2 A_1^2 + 4A_1^2\Omega^2 + \Omega^4}, \\
y =& \sqrt{\delta^2 + 2(2A_1^2 + \Omega^2 + x)}, \\
E_{00} =& \frac{(\delta - y)(\delta^2 + \Omega^2 + x + \delta y)}{2\Omega(2A_1^2 + \Omega^2 + x)}, \\
E_{01} =& \frac{A_1(\delta - y)}{2A_1^2 + \Omega^2 + x}, \\
E_{10} =& -\frac{A_1(\delta^2 + \Omega^2 + x + \delta y)}{\Omega(2A_1^2 + \Omega^2 + x)}.
\end{aligned}
\tag{D10}
$$

For brevity, the stabilized state $|\xi_{\delta, A_1}\rangle$ is not normalized. The form of the state is determined by two independent variables $\frac{\delta}{\Omega}$ and $\frac{A_1}{\Omega}$. We sweep these two variables and plot the simulated fidelity and purity in Fig. 10. This a general map covering all stabilized entangled states in the programmable operation: the vertical cut $\frac{\delta}{\Omega} = 0$ represents the blue line in case 2 Dressed parity Bell states, the horizontal cut $\frac{A_1}{\Omega} = 0$ represents the stabilized states shown in Fig. 1(b), and the bottom left point $(\frac{\delta}{\Omega}, \frac{A_1}{\Omega}) = (0, 0)$ is the even parity bell state $|\Psi_-\rangle$. Using a modest sideband rate combination, most of the states on the plot can be stabilized with fidelity over 90%. Correspondingly, changing the QQ sideband color to red can stabilize another 2D set of entangled states which are dual to this case. All possible programmable stabilization operations can be chosen accordingly through the map provided here. States with both $E_{01} > 1$ and $E_{10} > 1$ cannot be stabilized under this case for instance.

Appendix E: QR sideband colors and detunings

Changing sideband colors and detuning frequency signs stabilize different states. This is important for stabilizing $|\Psi_\theta\rangle$ and $|\Phi_\theta\rangle$: at certain blending angles the steady state fidelity is low because of the small effective refilling rate Γ_t (See Eq. 2).

As an explicit example, we consider the $|\Psi_\theta\rangle$ stabilization case. Instead of using two QR blue sidebands, we use two QR red sidebands with the same detuning and sideband rate. The rotating frame Hamiltonian now becomes

$$
\begin{aligned}
H_{\text{color}} =& \frac{\Omega}{2}\left(a_{q1}a_{q2} + h.c.\right) + \delta a_{q1}^\dagger a_{q1} \\
&+ \frac{W_1}{2}\left(a_{q1}^\dagger a_{r1} + h.c.\right) + \frac{W_2}{2}\left(a_{q2}^\dagger a_{r2} + h.c.\right) \\
&+ \frac{\Delta + \delta}{2}a_{r1}^\dagger a_{r1} + \frac{\Delta - \delta}{2}a_{r2}^\dagger a_{r2}.
\end{aligned}
\tag{E1}
$$

The four eigenenergies of the Hamiltonian can also be grouped into two pairs sharing the same sum. By appropriately choosing two QR sideband detunings, the lowest

Fig. 11 (a) shows the level diagram, where the QR red sidebands now connect $|ge00\rangle$ to $|\Psi_\theta 01\rangle$, which is different from the QR blue sidebands case where $|ge00\rangle$
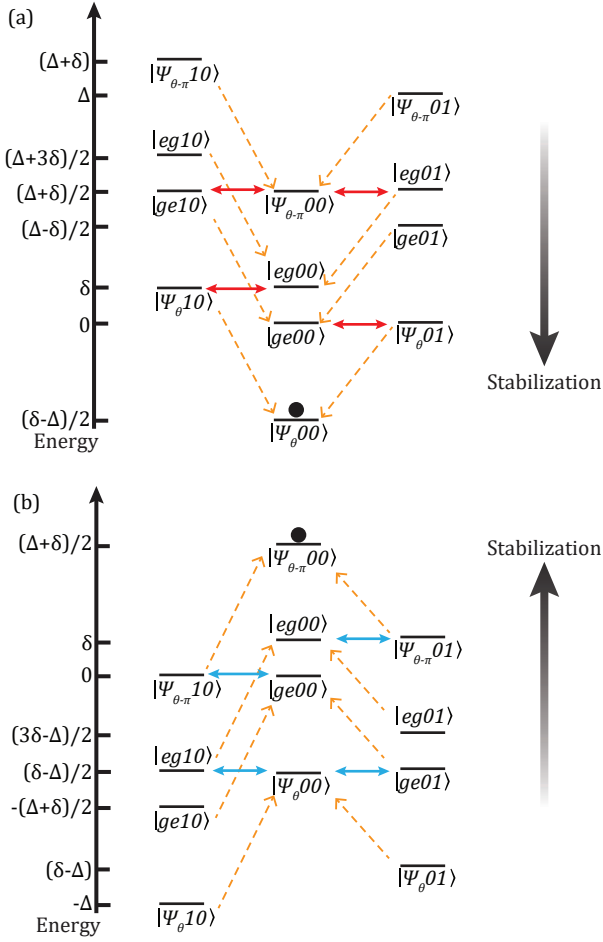
FIG. 11. (a) Use both QR red sidebands to stabilize $|\Psi_\theta\rangle$. (b) Use opposite QR blue sideband detunings to stabilize $|\Psi_{\theta-\pi}\rangle$. The QQ sideband rates and detunings are separate Ω and δ, and the QR sideband is detuned in frequency by $\frac{\Delta+\delta}{2}$, $\frac{\Delta-\delta}{2}$ in (a) and $-\frac{\Delta+\delta}{2}$, $-\frac{\Delta-\delta}{2}$ in (b). Here $\Delta = \sqrt{\Omega^2 + \delta^2}$.

and $|\Psi_\theta 10\rangle$ are connected. The two-step refilling rate Γ_{tc} for $|ge00\rangle \rightarrow |\Psi_\theta 00\rangle$ is

$$\Gamma_{tc} = \frac{W^2 \sin^2(\theta/2)\kappa}{\kappa^2 + W^2 \sin^2(\theta/2)}. \qquad (E2)$$

The other three two-step transitions $|eg00\rangle \rightarrow |\Psi_\theta 00\rangle$, $|\Psi_{\theta-\pi}00\rangle \rightarrow |ge00\rangle$, and $|\Psi_{\theta-\pi}00\rangle \rightarrow |eg00\rangle$ have the

same refilling rate. Therefore, the steady-state fidelity for $|\Psi_\theta\rangle$ is

$$\mathcal{F}_\infty = \left(\frac{\Gamma_t + \gamma \cos^2(\theta/2)}{\Gamma_t + \gamma}\right)^2. \qquad (E3)$$

One can thus choosing the QR sideband color for higher F_∞. When the F_∞ drops significantly near $\theta = \pi$ for Φ_θ stabilization case, one can flip the QR sideband color for better performance.

We can also keep the same QR sideband color while choosing opposite QR sideband detunings. The Hamiltonian becomes

$$\begin{aligned} H_{\text{opp}} =& \frac{\Omega}{2}(a_{q1}a_{q2} + h.c.) + \delta a_{q1}^\dagger a_{q1} \\ &+ \frac{W_1}{2}\left(a_{q1}^\dagger a_{r1} + h.c.\right) + \frac{W_2}{2}\left(a_{q2}^\dagger a_{r2} + h.c.\right) \\ &- \frac{\Delta+\delta}{2}a_{r1}^\dagger a_{r1} - \frac{\Delta-\delta}{2}a_{r2}^\dagger a_{r2}. \qquad (E4)\end{aligned}$$

The level diagram is shown in Fig. 11 (b). All population flows to $|\Psi_{\theta-\pi}\rangle$, with the same refilling rate (Eq. 2) and steady-state fidelity (Eq. 3) as the $|\Psi_\theta\rangle$ case.

Appendix F: Measurement setup

Figure 12 illustrates the measurement setup used in the experiment. Both single qubit, QR sidebands, and QQ sidebands signals are generated with a 4-channel AWG (Keysight M8195 65 Gsa/s, 16 Gsa/s per channel) to maintain phase-locking. DC flux bias for the coupler and two Josephson Parametric Amplifiers (JPAa) are generated with three current sources (Yokogawa GS200). The bandpass filters on both charge lines are chosen such that the stop band covers both readout and qubits' frequencies. The flux drive is delivered using three separate coaxial cables for DC bias, red sideband and blue sideband frequencies. The RF lines are merged using a combiner which is then added to the DC bias using a bias tee. The Stepped impedance Purcell filter (SIPF) inserted in the flux line is a home-made filter with a stop band between 2 GHz and 5.5 GHz blocking any qubit and resonator signals. Each transmitted signal is first amplified by a JPA with a +15 dB gain, followed by a HEMT amplifier and three room-temperature amplifiers. The final signal is pre-amplified after demodulation and digitized with an Alazar ATS 9870 (1GSa/s) card.

[1] F. Arute, K. Arya, R. Babbush, D. Bacon, J. C. Bardin, R. Barends, R. Biswas, S. Boixo, F. G. S. L. Brandao, D. A. Buell, B. Burkett, Y. Chen, Z. Chen, B. Chiaro, R. Collins, W. Courtney, A. Dunsworth, E. Farhi, B. Foxen, A. Fowler, C. Gidney, M. Giustina, R. Graff, K. Guerin, S. Habegger, M. P. Harrigan, M. J. Hartmann, A. Ho, M. Hoffmann, T. Huang, T. S. Humble, S. V. Isakov, E. Jeffrey, Z. Jiang, D. Kafri, K. Kechedzhi, J. Kelly, P. V. Klimov, S. Knysh, A. Korotkov, F. Kostritsa, D. Landhuis, M. Lindmark, E. Lucero, D. Lyakh, S. Mandrà, J. R. McClean, M. McEwen, A. Megrant, X. Mi, K. Michielsen,

M. Mohseni, J. Mutus, O. Naaman, M. Neeley, C. Neill, M. Y. Niu, E. Ostby, A. Petukhov, J. C. Platt, C. Quintana, E. G. Rieffel, P. Roushan, N. C. Rubin, D. Sank, K. J. Satzinger, V. Smelyanskiy, K. J. Sung, M. D. Trevithick, A. Vainsencher, B. Villalonga, T. White, Z. J. Yao, P. Yeh, A. Zalcman, H. Neven, and J. M. Martinis, Quantum supremacy using a programmable superconducting processor, Nature **574**, 505 (2019).

[2] Y. Wu, W.-S. Bao, S. Cao, F. Chen, M.-C. Chen, X. Chen, T.-H. Chung, H. Deng, Y. Du, D. Fan, M. Gong, C. Guo, C. Guo, S. Guo, L. Han, L. Hong, H.-L. Huang, Y.-H. Huo, L. Li, N. Li, S. Li, Y. Li, F. Liang, C. Lin, J. Lin, H. Qian, D. Qiao, H. Rong, H. Su, L. Sun, L. Wang, S. Wang, D. Wu, Y. Xu, K. Yan, W. Yang, Y. Yang, Y. Ye, J. Yin, C. Ying, J. Yu, C. Zha, C. Zhang, H. Zhang, K. Zhang, Y. Zhang, H. Zhao, Y. Zhao, L. Zhou, Q. Zhu, C.-Y. Lu, C.-Z. Peng, X. Zhu, and J.-W. Pan, Strong quantum computational advantage using a superconducting quantum processor, Phys. Rev. Lett. **127**, 180501 (2021).

[3] E. Kapit, P. Roushan, C. Neill, S. Boixo, and V. Smelyanskiy, Entanglement and complexity of interacting qubits subject to asymmetric noise, Phys. Rev. Res. **2**, 043042 (2020).

[4] F. Verstraete, M. M. Wolf, and J. Ignacio Cirac, Quantum computation and quantum-state engineering driven by dissipation, Nature Physics **5**, 633 (2009).

[5] E. Kapit, Hardware-efficient and fully autonomous quantum error correction in superconducting circuits, Phys. Rev. Lett. **116**, 150501 (2016).

[6] Y. Ma, Y. Xu, X. Mu, W. Cai, L. Hu, W. Wang, X. Pan, H. Wang, Y. P. Song, C.-L. Zou, and L. Sun, Error-transparent operations on a logical qubit protected by quantum error correction, Nature Physics **16**, 827 (2020).

[7] J. M. Gertler, B. Baker, J. Li, S. Shirol, J. Koch, and C. Wang, Protecting a bosonic qubit with autonomous quantum error correction, Nature **590**, 243 (2021).

[8] Z. Li, T. Roy, D. R. Perez, K.-H. Lee, E. Kapit, and D. I. Schuster, Autonomous error correction of a single logical qubit using two transmons (2023), arXiv:2302.06707 [quant-ph].

[9] Z. Li, T. Roy, D. R. Pérez, D. I. Schuster, and E. Kapit, Hardware efficient autonomous error correction with linear couplers in superconducting circuits (2023), arXiv:2303.01110 [quant-ph].

[10] S. Shankar, M. Hatridge, Z. Leghtas, K. M. Sliwa, A. Narla, U. Vool, S. M. Girvin, L. Frunzio, M. Mirrahimi, and M. H. Devoret, Autonomously stabilized entanglement between two superconducting quantum bits, Nature **504**, 419 (2013).

[11] M. E. Kimchi-Schwartz, L. Martin, E. Flurin, C. Aron, M. Kulkarni, H. E. Tureci, and I. Siddiqi, Stabilizing entanglement via symmetry-selective bath engineering in superconducting qubits, Phys. Rev. Lett. **116**, 240503 (2016).

[12] Y. Lu, S. Chakram, N. Leung, N. Earnest, R. K. Naik, Z. Huang, P. Groszkowski, E. Kapit, J. Koch, and D. I. Schuster, Universal stabilization of a parametrically coupled qubit, Phys. Rev. Lett. **119**, 150502 (2017).

[13] Z. Huang, Y. Lu, E. Kapit, D. I. Schuster, and J. Koch, Universal stabilization of single-qubit states using a tunable coupler, Phys. Rev. A **97**, 062345 (2018).

[14] C. K. Andersen, A. Remm, S. Lazar, S. Krinner, J. Heinsoo, J.-C. Besse, M. Gabureac, A. Wallraff, and C. Eich-

ler, Entanglement stabilization using ancilla-based parity detection and real-time feedback in superconducting circuits, npj Quantum Information **5**, 69 (2019).

[15] S.-l. Ma, X.-k. Li, X.-y. Liu, J.-k. Xie, and F.-l. Li, Stabilizing bell states of two separated superconducting qubits via quantum reservoir engineering, Phys. Rev. A **99**, 042336 (2019).

[16] C. C. Bultink, T. E. O'Brien, R. Vollmer, N. Muthusubramanian, M. W. Beekman, M. A. Rol, X. Fu, B. Tarasinski, V. Ostroukh, B. Varbanov, A. Bruno, and L. DiCarlo, Protecting quantum entanglement from leakage and qubit errors via repetitive parity measurements, Science Advances **6**, eaay3050 (2020), https://www.science.org/doi/pdf/10.1126/sciadv.aay3050.

[17] T. Brown, E. Doucet, D. Ristè, G. Ribeill, K. Cicak, J. Aumentado, R. Simmonds, L. Govia, A. Kamal, and L. Ranzani, Trade off-free entanglement stabilization in a superconducting qutrit-qubit system, Nature Communications **13**, 3994 (2022).

[18] Y. Lin, J. P. Gaebler, F. Reiter, T. R. Tan, R. Bowler, A. S. Sørensen, D. Leibfried, and D. J. Wineland, Dissipative production of a maximally entangled steady state of two quantum bits, Nature **504**, 415 (2013).

[19] D. C. Cole, S. D. Erickson, G. Zarantonello, K. P. Horn, P.-Y. Hou, J. J. Wu, D. H. Slichter, F. Reiter, C. P. Koch, and D. Leibfried, Resource-efficient dissipative entanglement of two trapped-ion qubits, Phys. Rev. Lett. **128**, 080502 (2022).

[20] S. Lloyd, M. Mohseni, and P. Rebentrost, Quantum principal component analysis, Nature Physics **10**, 631 (2014).

[21] M. Kjaergaard, M. E. Schwartz, A. Greene, G. O. Samach, A. Bengtsson, M. O'Keeffe, C. M. McNally, J. Braumüller, D. K. Kim, P. Krantz, M. Marvian, A. Melville, B. M. Niedzielski, Y. Sung, R. Winik, J. Yoder, D. Rosenberg, K. Obenland, S. Lloyd, T. P. Orlando, I. Marvian, S. Gustavsson, and W. D. Oliver, Demonstration of density matrix exponentiation using a superconducting quantum processor, Phys. Rev. X **12**, 011005 (2022).

[22] Y. Lu, Parametric control of flux-tunable superconducting circuits (2019).

[23] T. Roy, Z. Li, E. Kapit, and D. Schuster, Two-qutrit quantum algorithms on a programmable superconducting processor, Phys. Rev. Appl. **19**, 064024 (2023).

[24] E. Kapit, M. Hafezi, and S. H. Simon, Induced self-stabilization in fractional quantum hall states of light, Phys. Rev. X **4**, 031039 (2014).

[25] T. Roy, Z. Li, E. Kapit, and D. I. Schuster, Tomography in the presence of stray inter-qubit coupling (2021), arXiv:2103.13611.

[26] S. li Ma, J. Zhang, X. ke Li, Y. long Ren, J. kun Xie, M. tao Cao, and F. li Li, Coupling-modulation–mediated generation of stable entanglement of superconducting qubits via dissipation, Europhysics Letters **135**, 63001 (2021).

[27] A. Wallraff, D. I. Schuster, A. Blais, J. M. Gambetta, J. Schreier, L. Frunzio, M. H. Devoret, S. M. Girvin, and R. J. Schoelkopf, Sideband transitions and two-tone spectroscopy of a superconducting qubit strongly coupled to an on-chip cavity, Phys. Rev. Lett. **99**, 050501 (2007).
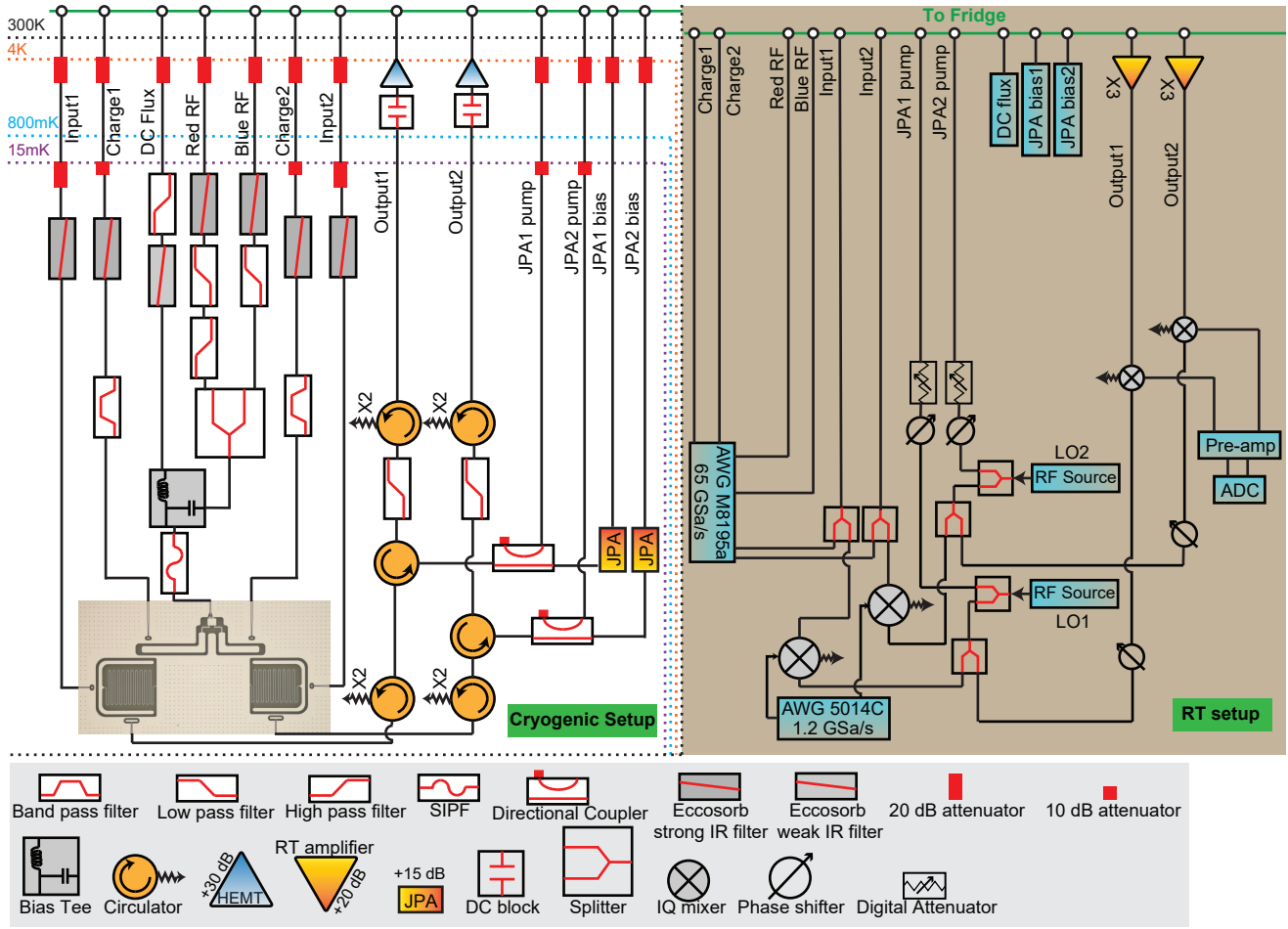
FIG. 12. Detailed measurement setup.